AIAA-01-2906

Effect of Cavitation on Vortex Dynamics in a Submerged Jet

T. Xing*and S. H. Frankel†
Maurice J. Zucrow Laboratories
School of Mechanical Engineering
Purdue University
West Lafayette, IN 47907

Abstract

The effects of cavitation on vortex dynamics in a submerged planar laminar forced jet were studied numerically. A locally homogeneous cavitation model that accounts for nonlinear bubble dynamics and bubble/bubble interactions within spherical bubble clusters was employed. The effects of varying key flow and cavitation model parameters on flow-cavitation interactions were investigated. The parameters varied include the cavitation number (vapor pressure), the bubble number density, the bubble-cluster radius, and the Reynolds number. The results showed cavitation occurring in the cores of primary vortical structures when the local pressure fell below the vapor pressure. Low levels of void fraction caused significant vortex distortion, with the details depending on the model parameters. For higher Reynolds numbers and small values of the bubble cluster radius, cavitation inhibited vortex pairing and resulted in vortex splitting. All of the above observations were in good qualitative agreement with previous experimental and numerical studies. The vorticity transport equation was used to examine the mechanisms behind the effects of cavitation on the vortex structures and it was found that both the dilatation and baroclinic torque terms played a role.

Introduction

Cavitation occurs in liquids when the local pressure drops below the saturated vapor pressure. This typically requires the presence of nucleation sites, which are usually small bubbles or air entrained within the fluid or trapped in solid crevices. In a flowing fluid, instabilities and turbulence often result in the formation of large-scale vortical structures. The pressure in the cores of these structures may fall below the local vapor pressure, providing favorable conditions for cavitation inception.[1–3] In addition, vapor formation also lowers the local density, which may have a significant effect on the local flow field. There have been a number of recent experimental and numerical studies examining flow-cavitation interactions, which serve to motivate the present study.

Sridhar *et al.*[4] examined the effect of entrained bubbles on the structure of vortex rings. Their experimental studies showed that the presence of only a few microscopic bubbles at very low void fraction can significantly effect the vortex dynamics within the impulsively started jets. When bubbles were entrained in the vortex ring they observed a shift and distortion of the vortex core, and depending on the number of bubbles and their relative locations within the vortex they also observed a splitting of the vortex and an intensification of the local vorticity. They explained these observations based on changes in the liquid momentum due to the presence of the vapor bubbles.

Gopalan *et al.*[5] conducted experimental studies of submerged water jets and showed cavitation occurring in the cores of either primary Kelvin-Helmholtz rollers or secondary streamwise vortical structures depending upon whether or not the jet was tripped at the nozzle exit. This highlights the sensitivity of jet cavitation to inlet conditions in experiments, industrial applications, or numerical simulations.

Cerutti *et al.*[6] compared predictions of cavitation inception rates in jets using an axisymmetric vorticity-stream function approach and a Lagrangian bubble tracking method. Results were in qualitative agreement with experimental observations of Gopalan *et al.*, although they did not consider the

*Doctoral Student
†Associate Professor, Senior Member AIAA

effect of the bubbles on the flow. These bubble-fluid interactions were recently shown to have a significant influence on energy distributions in free-shear flows.[7]

There have been a number of papers attempting to couple computational fluid dynamics solvers to various cavitation models in order to numerically study some of the above effects. The model of Kubota *et al.*[8] assumes homogeneous, isothermal, two-phase flow and accounts for the important effects of bubble dynamics by incorporating a modified version of the Rayleigh equation. The model accounts for bubble/bubble interactions within spherical bubble clusters distributed throughout the flow. The model neglects the mass and momentum of the vapor, the change of liquid mass due to phase change, and the changes in bubble number density as bubbles grow and decay. The model was applied to study unsteady cavitation on a hydrofoil section and produced reasonable results. More recently the model has been extended by Delale *et al.*[9] by relating the size of the bubble cluster radius to some multiple of the local bubble radius (assumed uniform throughout the cluster). When the cluster size is equal to the local bubble radius the model reverts back to the original Rayleigh equation for a single bubble, which does not account for bubble/bubble interactions. If the cluster size is greater than the local bubble radius, then the model relates the local number of bubbles to the local void fraction. This modifies the original assumption of constant bubble number density in the Kubota *et al.* model, to one of constant bubble number per unit mass. This latter assumption is more consistent with the modeling efforts of Chen and Heister *et al.*[10] Other modeling efforts include the two-fluid modeling work of Grogger and Alajbegovic,[11] the compressible flow model of Schmidt *et al.*,[12] and the volume of fluid model presented by Sauer *et al.*[13] and used in the FLUENT software.

In this work, the model of Kubota *et al.*,[8] henceforth referred to as Kubota's model, was employed to study cavitation in submerged planar jets. In particular, the focus was on the two-way coupling between the flow and the cavitation process. The choice of submerged planar jets was motivated by our interest in cavitation in hydraulic valves and the recent experimental evidence that such flows involve large-scale vortical structures which form as part of the unsteady turbulent jet flow.[14] In addition, several of the recent experimental studies of flow-cavitation interactions have involved free-shear flows, including jets, as already discussed.

Governing Equations

The following form of the Navier-Stokes equations were considered in this study:

$$\frac{\partial \rho}{\partial t} + \nabla \cdot (\rho \mathbf{V}) = 0 \tag{1}$$

$$\frac{\partial (\rho \mathbf{V})}{\partial t} + \nabla \cdot (\rho \mathbf{V}\mathbf{V}) = -\nabla p + 2\nabla \cdot (\mu \mathbf{S}) - \frac{2}{3}\nabla (\mu \nabla \cdot \mathbf{V}) \tag{2}$$

where $\mathbf{S}$ is the strain-rate tensor. The density of the liquid-vapor bubble mixture is defined as:

$$\rho = (1 - f_g)\rho_l \tag{3}$$

where ρ_l is the liquid density (the vapor density is assumed to be negligible compared to the liquid density) and f_g, the local void fraction, is defined as:

$$f_g = n\frac{4}{3}\pi R^3 \tag{4}$$

with $0 < f_g < 1$, n is the bubble number density, and R is the bubble radius. The mixture viscosity is evaluated using:

$$\mu = (1 - f_g)\mu_l + f_g \mu_g \tag{5}$$

where μ_l is the liquid viscosity and μ_g is the vapor viscosity, and both are assumed constant.

The bubble number density is assumed constant in both space and time, which limits the accuracy of the model for large void fractions by neglecting bubble coalescence and splitting. The Rayleigh equation governs the dynamic behavior of a single bubble in a quiescent medium.[3] Because grid resolution in most numerical simulations is insufficient to resolve individual bubbles, Kubota *et al.* modified the Rayleigh equation to account for interactions between bubbles (of the same radius, R), which may occur at scales below the grid scale. The final equation, referred to as the local homogeneous model (LHM) equation is given as:

$$(1+2\pi(\Delta r)^2 nR)R\frac{D^2R}{Dt^2} + \left(\frac{3}{2} + 4\pi(\Delta r)^2 nR\right)\left(\frac{DR}{Dt}\right)^2 + 2\pi(\Delta r)^2 \frac{Dn}{Dt}R^2\frac{DR}{Dt} = \frac{p_v - p}{\rho_l} \tag{6}$$

where D/Dt is the material derivative, Δr is the bubble cluster radius (distance over which bubbles may interact with each other in a given cluster), and p_v is the vapor pressure of the liquid for a given temperature. Surface tension, thermal, and viscous effects have been neglected in the above equation. Notice as the bubble cluster radius goes to zero, the

Rayleigh equation for a single bubble is recovered and bubble-bubble interactions are no longer included in the equation. Recently, Delale *et al.*[9] have revised Kubota's model and have addressed two important effects related to bubble/bubble interactions and viscous damping. In Kubota's original model, the bubble cluster radius is chosen to be the grid interval. In Delale *et al.*, they related the bubble cluster radius to the radius of the bubbles within the cluster itself (which is assumed the same for all bubbles within the cluster, but may grow or decay depending upon the local pressure) as follows:

$$\Delta r = \Lambda R \tag{7}$$

where $\Lambda = constant >> 1$ (if $\Lambda = 1$ then the classical Rayleigh equation is recovered). This model assumes that local number of bubbles within a cluster is proportional to the local volume of a bubble, and hence the local void fraction.

To couple the LHM equation for the bubble radius to the Navier-Stokes equations, Kubota *et al.* derived a quasi-Poisson equation for the pressure which is given below (for more details see reference[8]):

$$\nabla^2 p + \Theta(p) = \Phi(\rho\mathbf{V}, \mathbf{V}, \frac{\partial R}{\partial t}, R) + \Omega(\rho\mathbf{V}, \mathbf{V}) \tag{8}$$

with,

$$\Theta(p) = \rho_L 4n\pi R^2 \frac{p_v - p}{(1 + 2\pi(\Delta r)^2 nR)R\rho_L} \tag{9}$$

and,

$$\Phi(\rho\mathbf{V}, \mathbf{V}, \frac{\partial R}{\partial t}, R) = -\rho_L 4n\pi R\{R\theta(\rho\mathbf{V}, \mathbf{V}, \frac{\partial R}{\partial t}, R) + 2(\frac{\partial R}{\partial t})^2\} \tag{10}$$

with,

$$\Theta(\rho\mathbf{V}, \mathbf{V}, \frac{\partial R}{\partial t}, R) = \frac{\partial^2 R}{\partial t^2} - \Pi(p) \tag{11}$$

and,

$$\Pi(p) = \frac{p_v - p}{(1 + 2\pi(\Delta r)^2 nR)R\rho_L} \tag{12}$$

Maximum and minimum void fractions were specified to avoid pure liquid and vapor states with $\Theta = \Phi = 0$ with the bubble radius fixed. In the present implementation, a hyperbolic tangent function was used to ensure a smooth variation between these two extreme states. All quantities and equations were nondimensionalized by the liquid density and viscosity, the jet nozzle half-width, h, jet inlet velocity, U_0, and dynamic pressure, $\rho_l U_0^2$. In the results, all non-dimensional quantities will be indicated by an asterisk, *e.g.* t^*, x^*, u^*, etc..

Numerical Method

Kubota *et al.* integrated the above equations using a first-order Euler time integration with second-order central differences for spatial discretization. They had to include artificial dissipation to both the momentum and LHM equations. In this study, the momentum and LHM equations were spatially discretized using 6^{th} order compact central differences for interior points and 3^{rd} order compact scheme applied near or at the boundary of the computational domain.[15] The quasi-Poisson equation was discretized using 2^{nd} order central differences in order to facilitate implementation of the LSOR solver and the multigrid acceleration techniques.[16] Both 4^{th} order Runge-Kutta and first-order Euler time integration were considered, but the Euler time integration was chosen for computational efficiency. A 3^{rd} order explicit compact spatial filter was applied to the flow variables after each time step to eliminate spurious high-frequency numerical errors.

Problem Description

Recently, Gopalan *et al.* studied the flow structure in the near field of submerged water jets and its effect on cavitation inception. They found that for untripped jets cavitation inception occurred in the core of strong streamwise vortices, which formed just downstream of the nozzle exit. For tripped jets, the Kelvin-Helmholtz instability produced vortex roll-up and cavitation occurred in the cores of these, basically axisymmetric, vortical structures. Sridhar *et al.* studied the effect of entrained bubbles on vortex ring structure. They found that even a few bubbles at overall low void fraction could have a significant effect on the vortex ring structure. In certain instances, entrained bubbles distorted and split a single vortex into two structures and intensified the local vorticity. In our two-dimensional, planar cavitating jet simulations, we cannot simulate the untripped jet of Gopalan *et al.*, which features strong three-dimensional flow structures early in the jet, but we can, at least qualitatively, study the tripped jet case, which features unsteady vortex roll-up and cavitation. In addition, because our cavitation model accounts for the interaction between the bubble dynamics and the flow structure, we can also study the effect of cavitation (bubbles) on vortex dynamics and make qualitative comparisons to the experiments of Sridhar *et al.*.

Motivated by the above discussion, two-dimensional simulations of a planar submerged water jet exhausting into a chamber were conducted using the cavitation model, governing equations, and numerical methods previously described. A rectangular computational domain was chosen to represent the chamber. The jet was modeled just downstream of the nozzle by specifying a hyperbolic tangent velocity profile at the inlet with nondimensional momentum thickness of 0.32. A small amplitude sinusoidal disturbance was added to this base profile with Strouhal number of the primary frequency chosen as 0.223 and the secondary frequency was half this value. The nondimensional forcing period was 4.49. The jet Reynolds number was based on the nozzle half-width. For practical considerations regarding scaling effects, varying the Reynolds number is of interest. For the two-dimensional simulations considered here, varying the Reynolds number did not result in significant qualitative changes to the flow-cavitation interactions. In order to examine scaling effects associated with the Reynolds number and turbulence, experiments or three-dimensional large eddy simulations would be needed. This will be considered in future studies.

Another very important parameter for cavitating flows is the cavitation number. The cavitation number was defined here in terms of dimensional quantities as $\sigma = (p_\infty - p_v)/0.5\rho_l U_0^2$, where p_∞ is the chamber pressure. The cavitation number was varied by changing the vapor pressure. The ratio of the vapor to liquid viscosity was 0.00912 following Kubota *et al.*.

A sketch of the computational domain is given in Fig. 1. The computational domain extended from $-7.5 \leq y^* \leq 7.5$ in the transverse direction and $0 \leq x^* \leq 67$ in the streamwise direction. A nonuniform Cartesian grid with 513×129 points was employed. Grid stretching was used in the streamwise and transverse directions to facilitate resolution of the jet shear layers. Non-slip velocity boundary conditions were enforced at the top and bottom of the domain, with extrapolation for the pressure. At the outflow, a buffer domain extending from $40 \leq x^* \leq 67$ was employed which featured enhanced grid stretching (73 points were used in the axial direction in the buffer domain) and a smoothly vanishing viscosity. This resulted in a purely convective outflow condition, which tended to minimize spurious reflections.[17]

The simulation parameters considered here are presented in Table 1. Three different parameters were varied. These were the cavitation number σ (or equivalently the vapor pressure, p_v), the bubble number density, n, and the bubble-cluster radius, Δr. In addition, a non-cavitating case at the same Reynolds number was simulated for comparison purposes by lowering the vapor pressure to a value lower than that achieved by the flow anywhere in the computational domain. The simulations were run out to a nondimensional time of $t^* = 111.8$. Statistics were gathered for comparison purposes for a time period from $t^* = 40$ to $t^* = 111.8$, which is equal to 16 times the main forcing period.

Case	Re	σ	p_v	n	Δr
A	600	1.80	0.10	10^6	0.1
B	600	0.80	0.60	10^6	0.1
C	600	0.90	0.55	10^6	0.1
D	600	0.80	0.60	10^4	0.1
E	600	0.80	0.60	10^6	1.0
F	1000	1.80	0.10	10^6	0.2
G	1000	0.80	0.60	10^6	0.2

Table 1: Flow and cavitation model parameters for the simulation cases.

Results and Discussion

Grid and Domain Size

In order to assess the numerical accuracy of the simulations a grid refinement study was conducted. In addition, the effect of the domain size was examined by varying axial location of the outflow boundary. In the grid refinement study, the number of grid points in the vertical direction was roughly doubled. In the effect of the computational domain size study, the domain size was increased by 1.5 times in the streamwise direction. Figure 2 shows a transverse profile of the instantaneous axial velocity at x^*=20 from simulations with two different vertical grid sizes for Case B. The two profiles are similar suggesting adequate grid resolution (results were similar at other axial locations and times). Increasing the spatial extent of the computational domain in the axial direction did not change the results (not shown here). Hence, we employed the original domain and a grid size of 513×129 for all the results presented in the rest of the paper.

Cavitating vs. Non-cavitating Jets

In this section we compare simulation results for the non-cavitating case, Case A, with those for the cavitating case, Case B. The only difference between these two cases is the cavitation number. The overall effect of cavitation on the jet growth can be discerned from a plot of the axial variation of the momentum thickness shown in Fig. 3. Cavitation tends to suppress the jet growth in the first half of the jet in the region corresponding to $0 \leq x^* \leq 12$. This is followed by a rapid increase in the jet growth between $12 \leq x^* \leq 14$. Then the cavitating jet growth tends to level off. The location of the rapid increase in the growth of the jet at $x^* = 12$ roughly corresponds to the first location of vapor as determined from instantaneous contour plots (to be shown) and can be thought of as the location of cavitation inception. The jet growth suppression in the first half of the jet is then attributed to the decrease in density due to vapor formation stabilizing the jet. The rapid increase in jet growth downstream of this region is then related to pure expansion effects due to the presence of the vapor. This initial suppression followed by subsequent growth due to density variations is similar to the two-way coupling effects for the case of uniform bubble-phase concentration in a mixing layer.[18]

In Fig. 4 and 5, contour plots of instantaneous vorticity at three different times are compared for both cases. In Fig. 4, the Kelvin-Helmholtz vortex roll-up and pairing process can be clearly seen. In Fig. 5(a), the plot at nondimensional time $t^* = 44$, is similar to Fig. 4(a). At $t^* = 48$ and $t^* = 52$ differences in the vortical structure between the cavitating and non-cavitating cases can be seen. These differences are attributed to the presence of vapor near the cores of the second pair of vortical structures at $t^* = 44$ in Fig. 5. In order to quantify these differences, close-ups showing instantaneous velocity vectors, vorticity contours, and pressure contours are presented in Fig. 6 and 7 for the non-cavitating and cavitating cases, respectively. Due to cavitation, the location of the primary vortex core, as indicated by the center of the rotational flow pattern in the velocity vector plots, has shifted vertically upward approximately 0.15 and the core has expanded and the velocity has decreased. Cavitation appears to have to distorted and elongated the vortical structures. These observations are all in good qualitative agreement with the experimental findings reported by Sridhar and Katz.[4] The vortex pairing process has also been inhibited by cavitation, and an additional vortex can be seen in Fig. 5(b). Finally, the pressure in the core of the primary vortex is higher in the cavitating case as compared to the non-cavitating case. This is because when the local pressure falls below the vapor pressure, vapor formation in the cavitating cases serves to limit the lowest pressure within the flow field.

In order to observe cavitation inception and the unsteady fluctuations associated with cavitation, a comparison between the non-cavitating and cavitating cases, Case A and B, respectively, for the temporal evolution of the instantaneous pressure at a fixed point within the domain is shown in Fig. 11 (a). The point $x^* = 5.78, y^* = 1.75$ corresponds to a location where the vortex center passess. From this figure we can see that prior to $t^* = 42$, cavitation has not yet occurred since the minimum pressure within the domain has not yet dropped below the specified vapor pressure. Due to the elliptical nature of the quasi-Poisson pressure equation we can infer that there are no pressure fluctuations (hence vapor) anywhere else in the computational domain at this time. Hence, the pressure signals between the cavitating and non-cavitating cases are identical at this time. The low frequency pressure variations in both signals are due to the passing of a vortical structure. At $t^* = 42$, cavitation inception occurs when the local flow pressure drops below the vapor pressure (not necessarily at this location). As a result, high frequency pressure oscillations are observed to occur, which are indicative of bubble dynamics (alternative bubble growth and collapse) occurring somewhere in the domain. After $t^* = 46$, the oscillations disappear as the lowest pressure within the domain recovers above the vapor pressure.

Effect of Cavitation Number

The effect of cavitation number can be studied by comparing results from Cases B and C. The cavitation number was increased in Case C by decreasing the vapor pressure. All other parameters were the same between the two cases. In Fig. 8, close-ups of the vorticity and pressure contours for the same region as in Fig. 7 are shown. The velocity vector plots were similar for both cases and are not shown. The vorticity contours still reveal three main vortical regions although the magnitude of the vorticity

has decreased everywhere in the region shown. The pressure contours show that by lowering the vapor pressure, and hence increasing the cavitation number, the values of the pressure have decreased everywhere in the region shown. This is because the flow is able to reach a lower pressure before cavitation inception and vapor formation occur, which tends to limit the lowest pressure as already discussed in the comparison between Case A and B. If the vapor pressure is further decreased, eventually a single-phase or non-cavitating flow results. Increasing the cavitation number also tends to delay inception and decrease the amplitude of the pressure oscillations as shown in Fig. 11 (b).

Effect of Bubble Number Density

The bubble number density is a prespecified constant in Kubota's model. The actual value of this quantity may vary throughout the flow as a result of bubble coalescence and other effects. This is not accounted for in the current model. Therefore, it is of interest to examine the effect of this parameter on the interaction between cavitation and vorticity dynamics. In Case D, the bubble number density was decreased from 10^6 to 10^4 with all other parameters the same as in Case B (see Table 1). In Fig. 9, close-ups of the vorticity and pressure contours for the same region as in Fig. 7 are shown. Again, the velocity vector plots were similar for both cases and are not shown. The vorticity contours are qualitatively similar to the previous two cases, but are more similar to Case B than Case C. One interesting difference is the increase in the peak vorticity in the central vortex. The pressure is everywhere lower than in Case B in the region shown. By lowering the bubble number density everywhere in the domain, the amount of vapor formed due to cavitation, and hence the effect on the flow, is less noticeable. If the bubble number density is further decreased, a non-cavitating flow is recovered. This can also be seen in the further decrease in the pressure fluctuations as shown in Fig. 12(a).

Effect of Bubble Cluster Radius

The bubble cluster radius, Δr, is related to the spatial extent over which bubbles may interact with each other dynamically. In Case E, the bubble cluster radius is increased from 0.1 to 1.0 with all other parameters the same as in Case B. In Fig. 10, the vorticity contours reveal only two main vortical structures, most similar to the non-cavitating case (Case A) but with lower peak values for the vorticity. The pressure is everywhere lower than in Case B, but higher than in Case A. Increasing the bubble cluster radius, increases the amount of diffusion associated with the LHM equation. This damping effect can be revealed in Fig. 13, which shows the temporal evolution of the maximum void fraction for Cases B and E. With a smaller bubble cluster radius in Case B, the void fraction increases and decreases with a much higher frequency than that in Case E. This is consistent with the recent findings of Delale *et al.*[9] This damping effect can also be seen in the virtual elimination of pressure fluctuations as shown in Fig. 12(b).

Vorticity Transport Equation Analysis

In order to get a better understanding of the effect of cavitation on vorticity dynamics it is useful to examine the vorticity transport equation shown below:

$$\frac{D\omega}{Dt} = \omega \cdot \nabla \mathbf{V} - \omega \nabla \cdot \mathbf{V} + \frac{\nabla \rho \times \nabla p}{\rho^2} + \nu \nabla^2 \omega \quad (13)$$

The vorticity of a fluid particle can be changed by the various terms on the right hand side of this equation, which are, from left to right, vortex stretching (zero in this two-dimensional flow), dilatation, baroclinic torque, and viscous diffusion. Fig. 14 shows plots of the instantaneous (a) void fraction along with the (b) dilatation and (c) baroclinic torque terms (both with sign) from the vorticity transport equation. Both the dilatation and the baroclinic torque terms are non-zero in the same general vicinity of the non-zero void fraction region. Notice that these terms can act as both a source and a sink for vorticity.

Effect of Reynolds Number

It has been observed in the experiments of Sridhar *et al.*[4] that for the appropriate number and sizes of bubbles entrained by a vortex, a splitting of the vortex into two separate regions was observed with

significant increase in the peak vorticity in each region. In order to capture this phenomena, results are presented here from Case G, where the Reynolds number was increased from 600 to 1000 and the bubble cluster radius was 0.2. All other parameters were the same as in Case B. A non-cavitating case, Case F, was also studied for this same Reynolds number. In Fig. 15 (c) and Fig. 16 (c), close-ups of velocity vectors (with $0.6U_0$ subtracted from each vector to highlight the flow pattern) in the region where vapor was present are shown. In the non-cavitating Case F, a single vortex can be discerned, whereas for the cavitating Case G, the vortex has split into two separate vortices with the same sign. This is consistent with previous numerical simulations of Loth.[19] The peak vorticity in this region has decreased compared to the non-cavitating case. These results suggest that cavitation may inhibit the vortex pairing process, hence stabilizing the jet and effecting the distribution and levels of turbulent kinetic energy. Further experimental measurements and three-dimensional large eddy simulations would be required to investigate this.

Conclusions

Numerical simulations of cavitation in planar submerged laminar jets were conducted. The effects of cavitation and vapor formation on the liquid flow was accounted for in the model. The key flow and cavitation model parameters were varied to study their effect. The processes of vortex roll-up and pairing were effected by the presence of vapor associated with the cavitation process. Specific findings were as follows:

- Cavitation occurred in the cores of the vortical structures when the local pressure fell below the vapor pressure.
- Cavitation suppressed jet growth upstream of the location of the first vortex pairing and enhanced jet growth after the pairing.
- Cavitation caused the location of the vortex core to shift vertically away from the jet axis.
- Cavitation inhibited the vortex pairing process.
- Cavitation tended to distort and elongate the vortical structures.
- Cavitation set a lower limit for the pressure.
- Increasing the cavitation number or decreasing the bubble number density weakened the effects of cavitation.
- Increasing the bubble cluster radius increased damping effects and decreased both the amplitude and frequency of the pressure and void fraction fluctuations.
- Increasing the Reynolds number with vapor formation at the center of vortex caused the vortex to split into two disjointed vortices with the same sign.

Extensions of the present flow model to three-dimensions and inclusion of a subgrid-scale turbulence model will allow large eddy simulations to be conducted for cavitating jet flows with quantitative comparison to experimental data.

Acknowledgments

The authors would like to gratefully acknowledge Caterpillar Inc., Peoria, Illinois for their financial support of this research.

References

[1] Arndt, R. E. A., Cavitation in fluid machinery and hydraulic structures, *Ann. Rev. Fluid Mech*, **13**:273–328 (1981).

[2] Rood, E. P., Review - mechanisms of cavitation inception, *J. Fluids Engineering*, **113**:163–175 (1991).

[3] Brennen, C. E., Spherical Bubble Dynamics, in *Cavitation and Bubble Dynamics*, New York, Oxford, 1995, Oxford University Press.

[4] Sridhar, G. and Katz, J., Effect of Entrained Bubbles on the Structure of Vortex Rings, *J. Fluid Mech.*, **397**:171–202 (1999).

[5] Gopalan, S., Katz, J., and Knio, O., The flow structure in the near field of jets and its effects on cavitation inception, *J. Fluid Mech.*, **398**:1–43 (1999).

[6] Cerutti, S., Knio, O. M., and Katz, J., Numerical study of cavitation inception in the near field of an axisymmetric jet at high Reynolds number, *Physics of Fluids*, **12, n10**:2444–2460 (2000).

[7] Rightley, P. M. and Lasheras, J. C., Bubble dispersion and interphase coupling in a free-shear flow, *J. Fluid Mech.*, **412**:21–59 (2000).

[8] Kubota, A., Kato, H., and Yamaguchi, H., A new modelling of cavitating flows: a numerical study of unsteady cavitation on a hydrofoil section, *J. Fluid Mech.*, **240**:59–96 (1992).

[9] Delale, C. F., Schnerr, G. H., and Sauer, J., Quasi-one-dimensional steady-state cavitating nozzle flows, *J. Fluid Mech.*, **427**:167–204 (2001).

[10] Chen, Y. and Heister, S. D., Modeling hydrodynamic nonequilibrium in cavitating flows, *J. of Fluids Engineering*, **118**:172–178 (1996).

[11] Grogger, H. A. and Alajbegovic, A., Calculation of the cavitating flow in venturi geometries using two fluid model, in *Proceedings of the Fluids Engineering Division Summer Meeting, FEDSM98-5295*, pp. 1–6, ASME, 1998.

[12] Schmidt, D. P., Rutland, C. J., Corradini, M. L., Roosen, P., and Genge, O., Cavitation in two-dimensional asymmetric nozzles, SAE Congress 1999-01-0518, SAE, 1999.

[13] Sauer, J. and Schnerr, G. H., Unsteady cavitating flow - a new cavitation model based on a modified front capturing method and bubble dynamics, in *2000 ASME Fluids Engineering Division Summer Meeting FEDSM2000-11095*, ASME, 2000.

[14] Kanno, T., Aoki, T., Takahashi, K., and Nonoshita, T., Study of Flow in a Spool Valve, *ASME FED*, **207**:87–92 (1995).

[15] Lele, S. K., Compact Finite Difference Schemes with Spectral-like Resolution, *Journal of Computational Physics*, **103**:16–42 (1992).

[16] Briggs, W. L., Elements of Multigrid, in *A Multigrid Tutorial*, Pennsylvania, ISBN 0-89871-221-1, 1987, Lancaster Press.

[17] Liu, C. and Liu, Z., Multigrid Methods and High Order Finite Difference for Flow in Transition, in *11th AIAA Computational Fluid Dynamics Conference*, pp. 615–641, AIAA, July 6-9, 1993.

[18] Druzhinin, O. A. and Elghobashi, S. E., Direct numerical simulation of a three-dimensional spatially developing bubble-laden mixing layer with two-way coupling, *J. Fluid Mech.*, **429**:23–61 (2001).

[19] Loth, E., Boris, J. P., and Emery, M., Very Large Bubble Cavitation in a Temporally-Evolving Free Shear Layer, in *1998 ASME Fluids Engineering Division Summer Meeting FEDSM98-5028*, pp. 1–8, ASME, 1998.

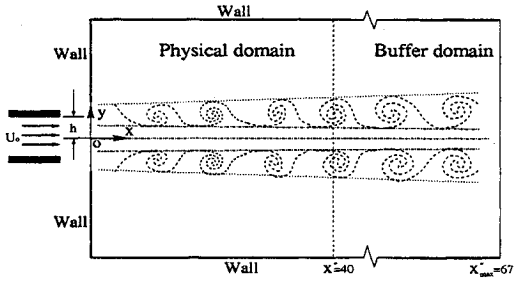

Figure 1: Sketch of the computational domain.

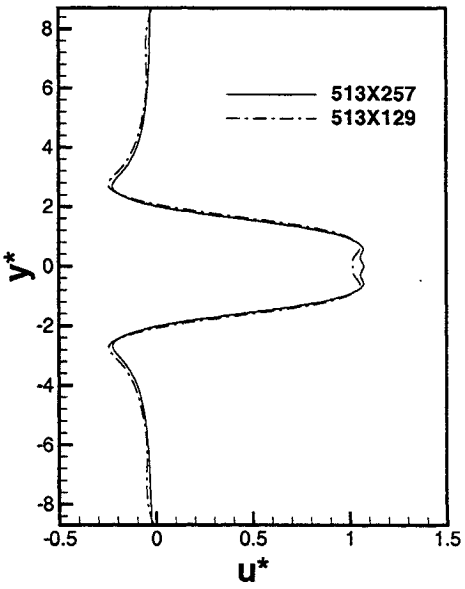

Figure 2: Instantaneous axial velocity profiles at t^*=40 for two different transverse grid sizes.

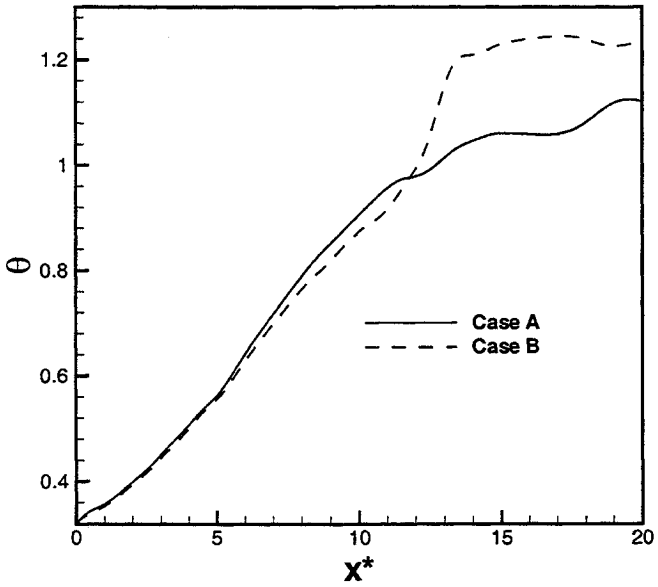

Figure 3: Effect of cavitation on momentum thickness versus axial distance for non-cavitating Case A and cavitating Case B.

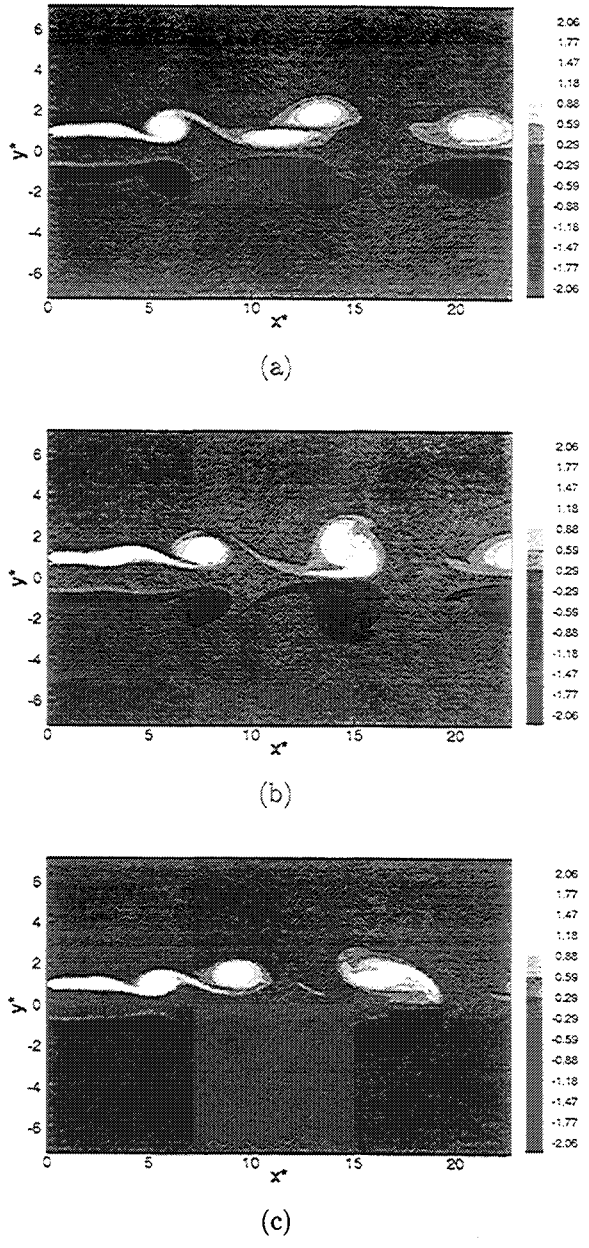

Figure 4: Contour plots of instantaneous vorticity for the non-cavitating case, Case A (a) t^*=44, (b) t^*=48, and (c) t^*=52.

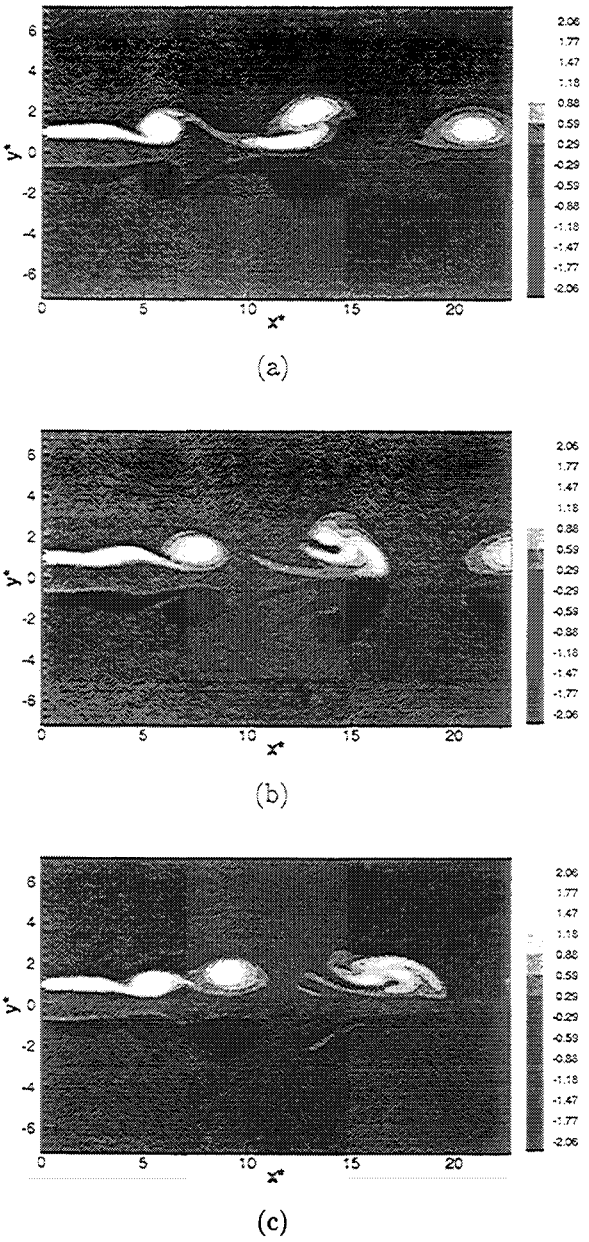

Figure 5: Contour plots of instantaneous vorticity for cavitating case, Case E (a) t^*=44, (b) t^*=48, and (c) t^*=52.

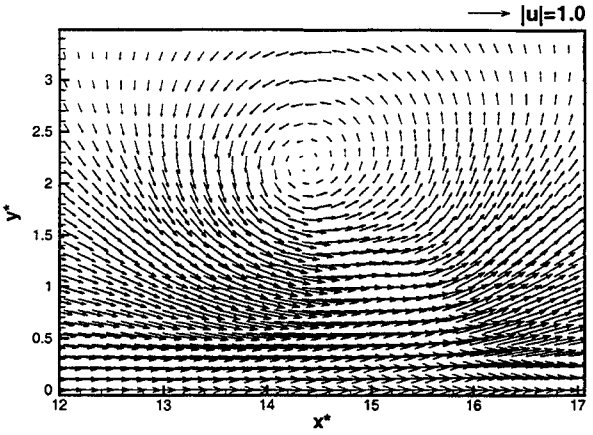

(a)

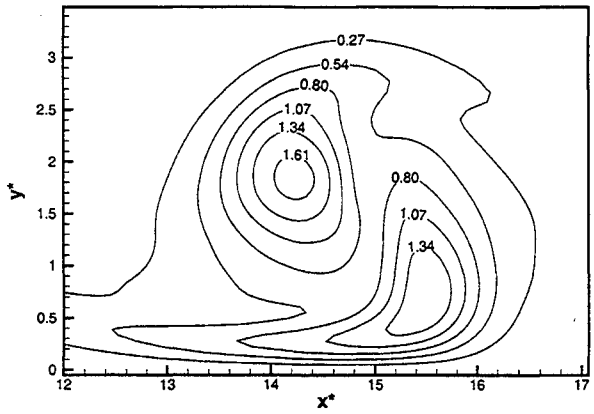

(b)

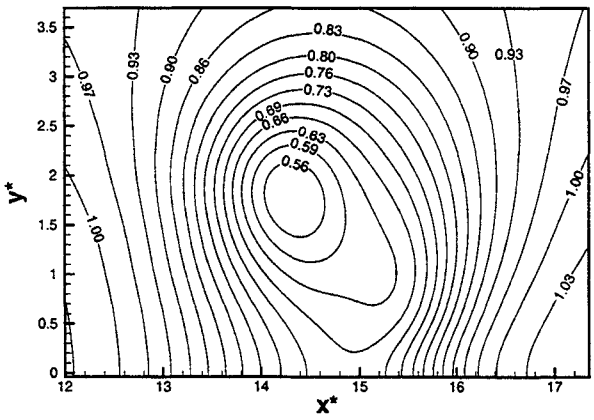

(c)

Figure 6: Close-up of instantaneous (a) velocity vectors, (b) vorticity contours, and (c) pressure contours at t^*=48 for the non-cavitating case, Case A.

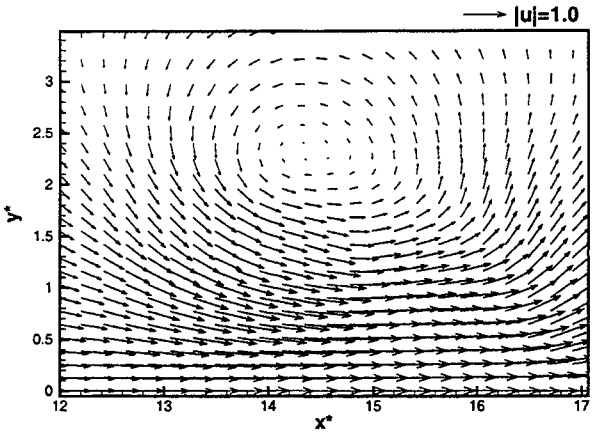

(a)

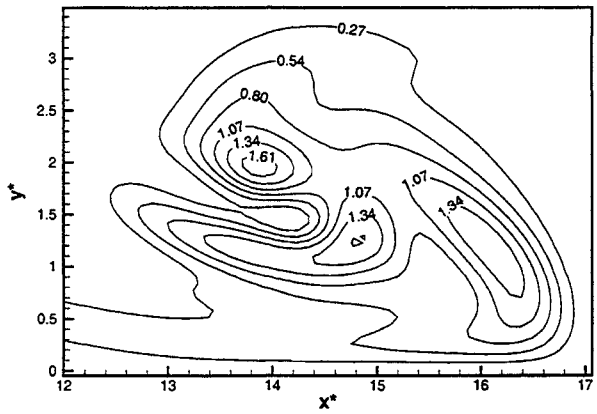

(b)

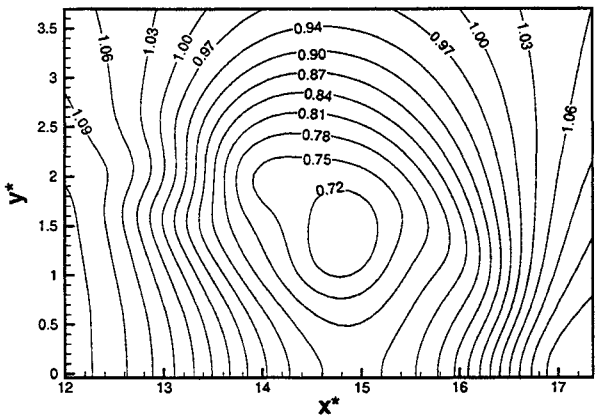

(c)

Figure 7: Close-up of instantaneous (a) velocity vectors, (b) vorticity contours, and (c) pressure contours at t^*=48 for the cavitating case, Case B.

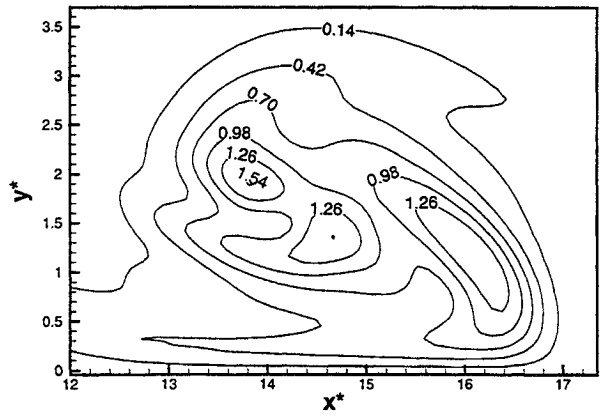

(a)

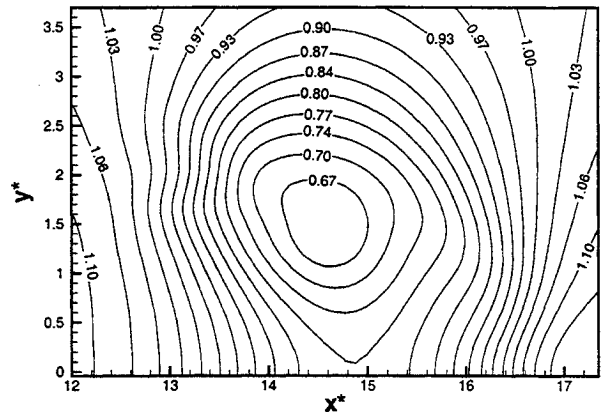

(b)

Figure 8: Close-up of instantaneous (a) vorticity and (b) pressure contours at t^*=48 for the cavitating case, Case C.

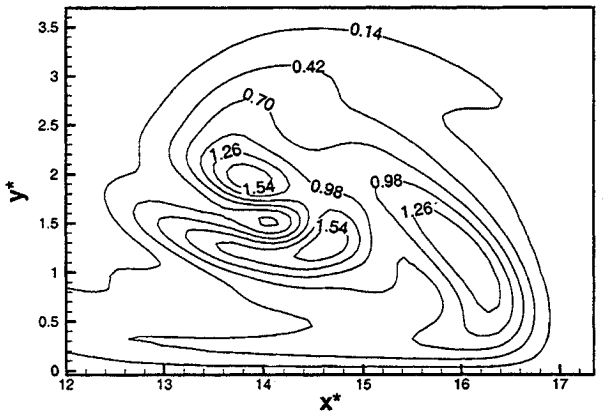

(a)

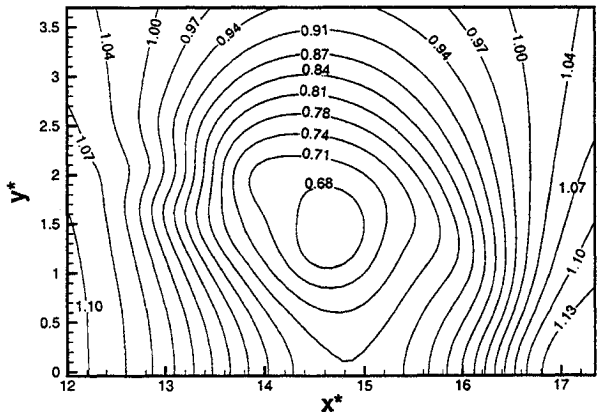

(b)

Figure 9: Close-up of instantaneous (a) vorticity and (b) pressure contours at t^*=48 for the cavitating case, Case D.

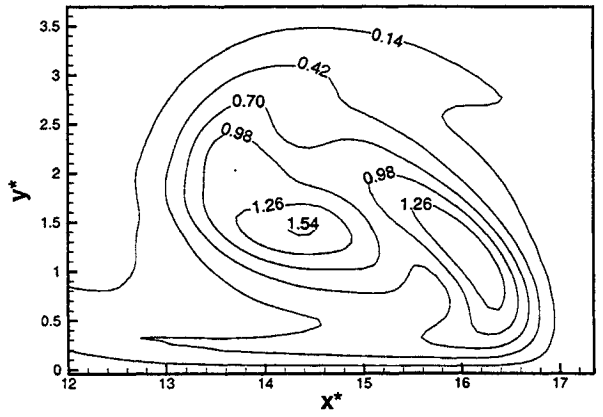

(a)

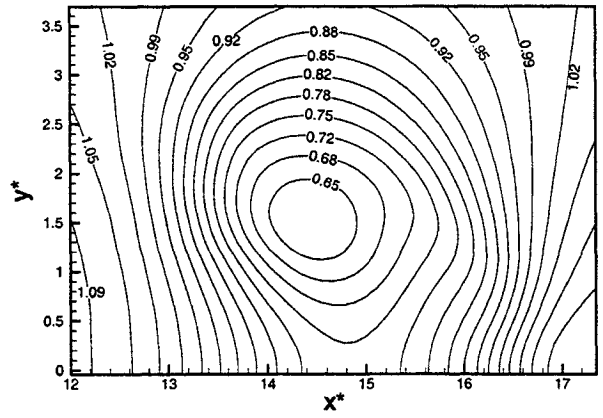

(b)

Figure 10: Close-up of instantaneous (a) vorticity and (b) pressure contours at t^*=48 for the cavitating case, Case E.

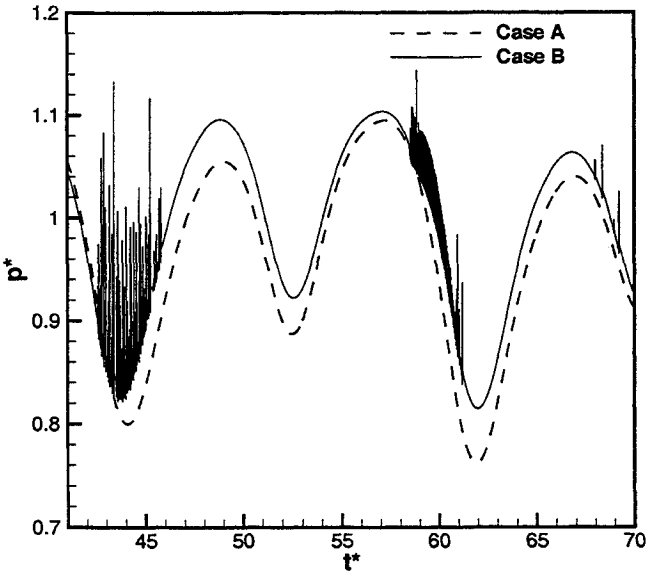

(a)

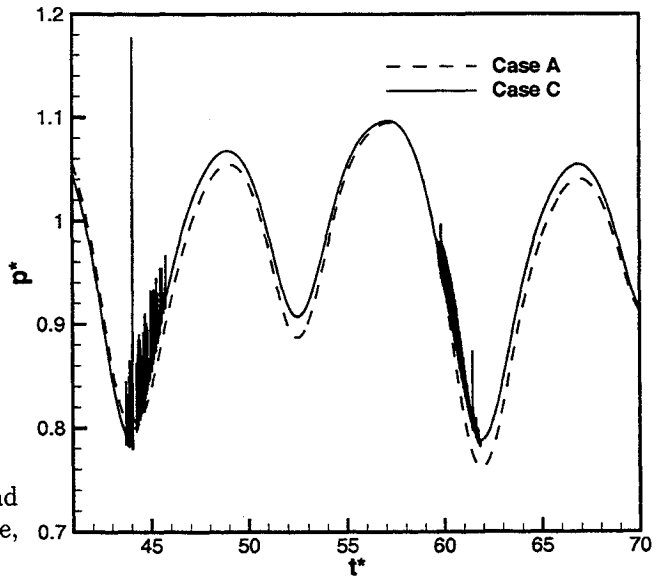

(b)

Figure 11: Temporal evolution of instantaneous pressure at one fixed point for (a) Case B and (b) Case C.

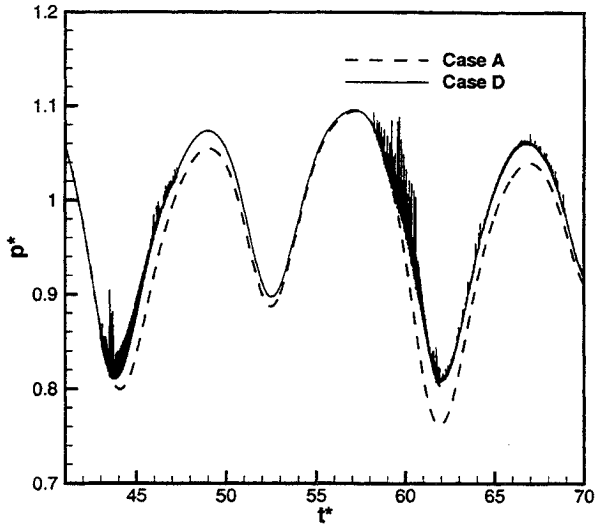

(a)

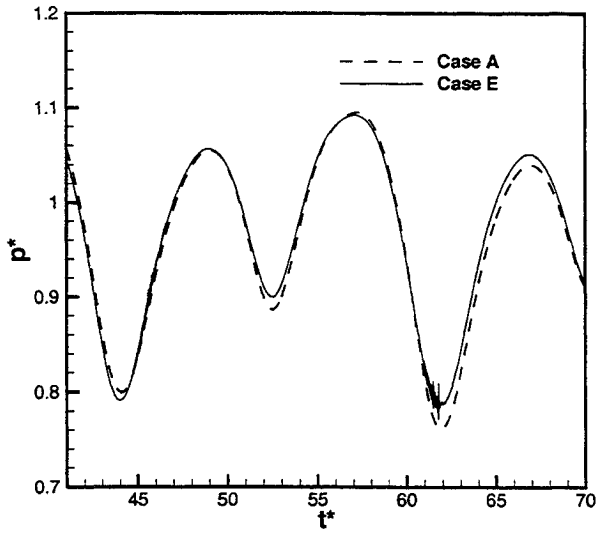

(b)

Figure 12: Temporal evolution of instantaneous pressure at one fixed point for (a) Case D and (b) Case E.

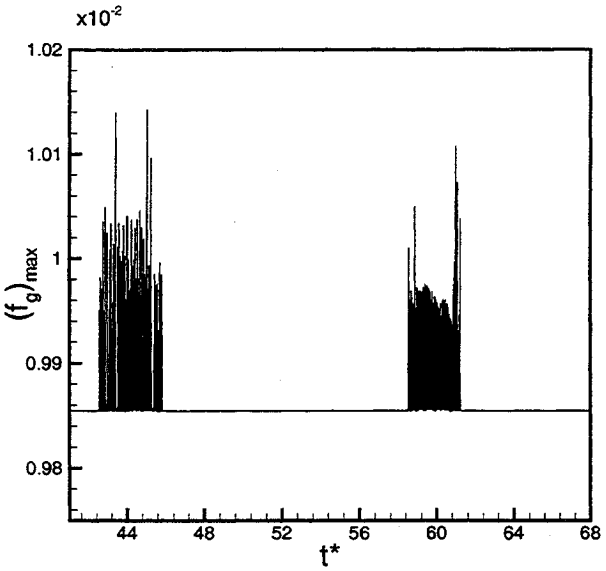

(a)

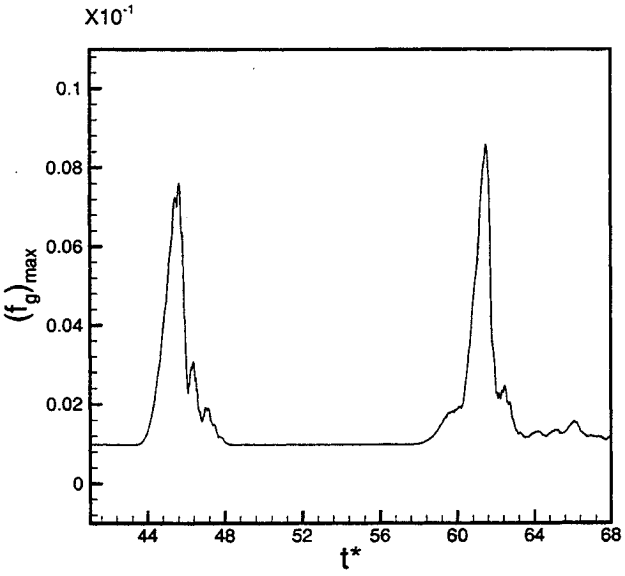

(b)

Figure 13: Temporal evolution of maximum void fraction for (a) Case B and (b) Case E.

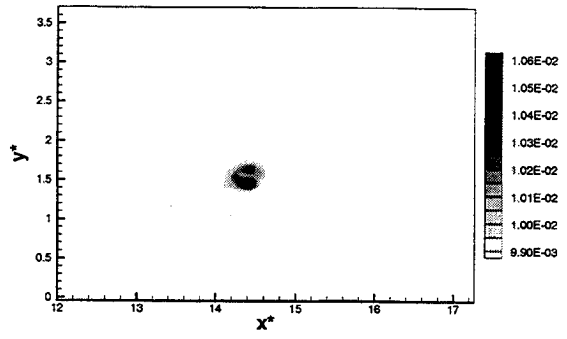

(a)

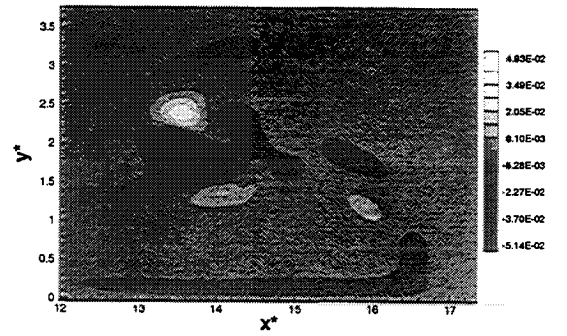

(b)

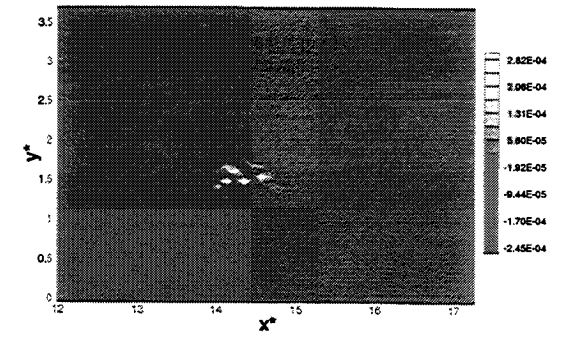

(c)

Figure 14: Close-up of instantaneous (a) void fraction, (b) expansion term, and (c) baroclinic torque term at t^*=48 for the cavitating case, Case E.

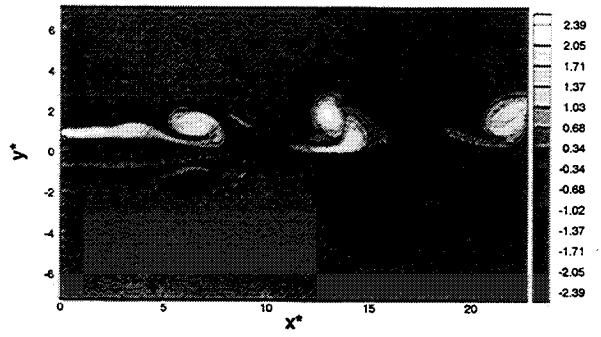

(a)

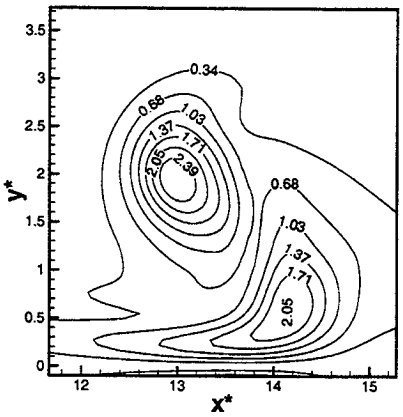

(b)

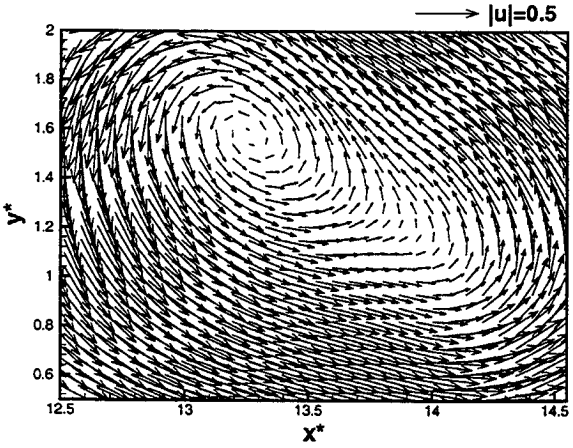

(c)

Figure 15: Instantaneous contour plot of (a) vorticity and close-up of (b) vorticity and (c) velocity vectors at t^*=54 for non-cavitating case, Case F.

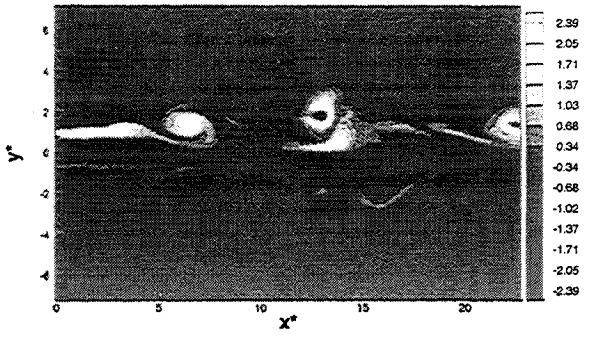

(a)

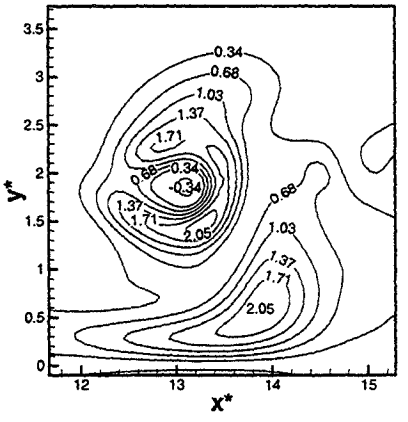

(b)

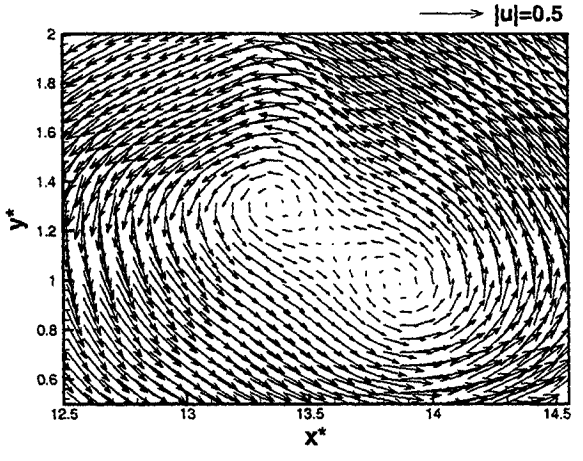

(c)

Figure 16: Instantaneous contour plot of (a) vorticity and close-up of (b) vorticity and (c) velocity vectors at t^*=54 for cavitating case, Case G.